Driven transport of fluid vesicles through narrow pores

G. Gompper[1] and D.M. Kroll[2]
[1]*Max-Planck-Institut für Kolloid und Grenzflächenforschung, Kantstrasse 55, 14513 Teltow, Germany and Sektion Physik der Ludwig-Maximilians-Universität München, Theresienstrasse 37, 80333 München, Germany*
[2]*Department of Medicinal Chemistry and Minnesota Supercomputer Institute, University of Minnesota, 308 Harvard Street Southeast, Minneapolis, Minnesota 55455*
(Received 26 May 1995)

The driven transport of fluid vesicles through narrow, cylindrical pores in a linear external potential is studied using Monte Carlo simulations, scaling arguments, and mean-field theory. The mobility of the vesicles increases sharply when the strength f of the driving field exceeds a threshold value f^*. For $f > f^*$, the mobility saturates at a value that is essentially independent of the strength of the driving field. The threshold field strength f^* is found to scale with the membrane bending rigidity κ, the vesicle area A_0, and the pore size r_p as $f^*/k_BT \sim (\kappa/k_BT)^{1+\beta} A_0^{-3/2+\eta} r_p^{-2\eta}$. An analysis of the zero-temperature limit yields the exponents $\beta = 0$ and $\eta = 1.55$, while the Monte Carlo simulations of low-bending-rigidity vesicles are well described by the (effective) exponents $\beta \simeq 0.2$ and $\eta \simeq 2.4$.

PACS number(s): 05.40.+j, 64.60.Fr, 87.22.Bt

I. INTRODUCTION

Lipid bilayer vesicles have been studied intensively recently [1,2]. It is now generally accepted that the shape and fluctuation spectra of vesicles are controlled by the bending energy [3–5]

$$\mathcal{H}_{curv} = \int dS \left[\frac{1}{2}\kappa(C_1 + C_2)^2 + \bar{\kappa} C_1 C_2\right] \qquad (1)$$

of the membrane, where C_1 and C_2 are the two principal curvatures, and the integral extends over the vesicle surface. The interplay between the bending elasticity and constraints on the volume or the mean curvature gives rise to a large variety of equilibrium shapes [6–10]. On the other hand, the fact that membranes are tensionless makes them very "soft," so that vesicles can be deformed easily by external forces. For example, red blood cells can squeeze through narrow capillaries of diameter less than their size [11], and artificial, ultraflexible vesicles (transfersomes) have been shown to be able to transport drugs such as insulin through the intact skin [12–14].

In this paper we study the driven diffusion of vesicles through narrow, cylindrical pores. The energy E_{cyl} required to deform a spherical vesicle of radius r_v to fit into a tube of radius r_p is $E_{cyl} \sim \kappa(r_v/r_p)^2$ for $r_v \gg r_p$. For pure lipid bilayers, the bending rigidity κ is typically on the order of $10k_BT - 20k_BT$, so that the probability that thermal fluctuations can overcome this barrier is extremely small. A driving field is therefore required to pull (or push) the vesicle through the pore. This can be a hydrostatic or osmotic pressure gradient, or an electric field. In many applications, such as transdermal drug delivery [12–14], this driving field is rather small. On the other hand, large field gradients could easily rupture the vesicle membrane [15,16]. Optimal efficiency therefore requires that the bending rigidity κ of the vesicle be on the order of k_BT.

Ultraflexible vesicles with an effective bending rigidity on the order of the thermal energy can be obtained when the lipid bilayer consists of a mixture of two or more components with different "spontaneous curvatures." Such composite membranes can still be described by the Hamiltonian (1), but with an effective bending rigidity which depends on the concentrations and spontaneous curvatures of the lipid components [17–19]. This reduction of the bending rigidity can easily be understood intuitively: the lipid species which better adapts to large curvatures accumulates in strongly deformed regions, thereby reducing the energy cost of vesicle deformation.

In this paper we study the driven diffusion of vesicles in a constant field gradient through a cylindrical tube with a periodic array of narrow (cylindrical) segments. This corresponds, for example, to the transport of uniformly charged vesicles driven by a constant electric field [20]. We assume that the field strength is sufficiently small that the transport is slow compared to the time scale of thermal fluctuations of the membrane, so that hydrodynamic effects can be neglected. Furthermore, the volume of the vesicle is free to adjust to the external conditions. The situation usually studied in experiments, however, is a vesicle suspension which is driven by a hydrostatic pressure difference through a thin, porous material [14]. In this case, the flow field at the entrance of the pores may already elongate the vesicles [21] so that they can slip into the pores more easily. On the other hand, if the rate of solvent exchange across the membrane is slow enough, the vesicle mobility could be reduced. A more detailed comparison with experiment will be published elsewhere [22].

How does the permeability of a vesicle suspension depend on the strength of the driving field, the vesicle's bending rigidity κ, its size r_v, and the pore radius r_p? In

this paper we address this question using Monte Carlo simulations, scaling argument, and mean-field theory. Our analysis is based on the curvature Hamiltonian (1) for a vesicle with surface area A. The driving field is modeled by an additional potential energy contribution

$$\mathcal{H}_{pot} \equiv f \int dS\ z \tag{2}$$

to the vesicle free energy. In Sec. II we present Monte Carlo results for the transport of a single vesicle down a tube composed of a sequence of wide and narrow regions. It is shown that transport occurs via a sequence of nucleation processes, and the scaling behavior of the threshold field strength f^* at which the nucleation barrier vanishes is described. Section III contains an analysis of the zero-temperature limit. The scaling form of f^* is derived, and the scaling exponents are determined numerically. Fluctuation effects are discussed briefly in Sec. IV. The paper closes in Sec. V with a short summary and discussion.

II. MONTE CARLO SIMULATIONS

We have performed extensive Monte Carlo simulations of the transport of simple model vesicles in a cylindrical geometry in order to study the dependence of the mobility on the pore radius, the vesicle size, and the bending rigidity. The lipid membrane is modeled by a triangular network of N spherical beads of diameter σ_0, which are connected by flexible tethers of length $\ell < \sqrt{3}\sigma_0$. This constraint on the tether lengths guarantees self-avoidance. In our simulations, we use $\sigma_0 = 1$ and $\ell = \sqrt{2.8}\sigma_0$. In order to allow for diffusion within the membrane, tethers can be cut and reattached between the four beads which form two neighboring triangles. The bending energy is approximated by the scalar product of normal vectors $\mathbf{n}_i$ and $\mathbf{n}_i$ of neighboring triangles i and j,

$$\mathcal{H}_{curv} = \lambda \sum_{\langle ij \rangle} (1 - \mathbf{n}_i \cdot \mathbf{n}_j)\ , \tag{3}$$

where $\lambda = \sqrt{3}\kappa$ [23]. We consider a single vesicle confined to a tube of radius R (more precisely, the *center of mass* of each bead is confined to the interior of the tube). The tube has narrow regions, in which the radius is reduced to r_p. The length of the narrow regions, as well as the distance between them, is L. Finally, the driving field is modeled by the linear potential fz_k, where z_k is the z coordinate of bead k, so that

$$\mathcal{H} = \mathcal{H}_{curv} + f\sigma_0^2 \sum_k z_k\ . \tag{4}$$

Here, the z direction is parallel to the long axis of the tube. The simulations are performed using the standard Metropolis algorithm. A Monte Carlo step (MCS) consists of an attempt to update the positions of all N beads by a random increment in the cube $[-s, s]^3$, followed by N attempted tether cuts. More details concerning the simulation procedure can be found in Ref. [23]. We do not pose any constraints on the volume of the vesicle. By construction, our model vesicles can never be torn apart.

The motion of a vesicle along the tube can be described by monitoring the position of its center of mass as a function of Monte Carlo time (measured in units of attempted moves per bead). A typical transport curve is shown in Fig. 1. In the wide portions of the tube, the vesicle moves with a velocity proportional to the strength of the driving field. It slows down when it reaches the entrance of the pore. After an f-dependent waiting time, it slips into the narrow portion of the tube (compare Fig. 2). As soon as it is inside the pore, it moves with approximately the same velocity as outside the pore; after a while, the vesicle leaves the pore region, and the whole process starts all over again. We calculate the average velocity of a vesicle typically from runs of $(10\text{–}50)\times 10^6$ Monte Carlo steps per bead, which corresponds to the passage of up to 40 pores in sequence. Since the vesicle is forced to take the shape of a long cylinder inside the pore, its volume V is reduced compared to the average volume outside the pore. This can be seen, for example, from the bimodal shape of the volume distribution $P(V)$, which is shown in Fig. 3 for the smallest pore radius we have studied in our simulations. Note that for the bending rigidities and pore sizes used here, the motion of the vesicle is slow compared to other characteristic time scales, such as the typical relaxation time for shape fluctuations. It should therefore be justified to neglect hydrodynamic effects, as we did in our simulations.

The quantity we determine from the simulations is the mobility μ of the vesicle, which is given by the velocity of the center of mass divided by the total driving force $N\sigma_0^2 f$. Since the mobility of a free vesicle scales as $1/N$, we show in Fig. 4 the reduced mobility $N\mu$ [measured in units of $\sigma_0^2/(k_BT)$ per 10^6 MCS] as a function of the driving field for $N = 127$, $\lambda/k_BT = 1.0$, and several different pore sizes. The lower limit of field strengths f we can study is reached when the waiting time at the pore entrance is of the same order as the total time of a simulation run. With increasing f, the mobility rapidly increases, until, for large driving fields, it reaches a plateau

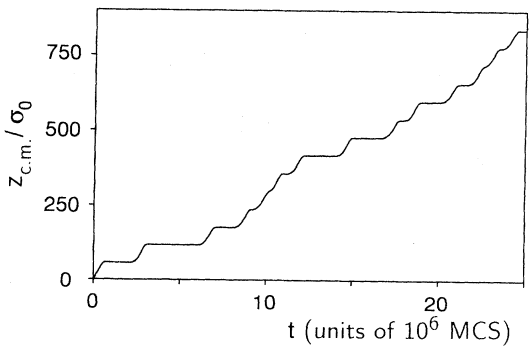

FIG. 1. The position of the center of mass, $z_{c.m.}$, of a vesicle of size $N = 407$ and bending rigidity $\lambda = 2.0k_BT$, moving in a tube with pore radii $R = 9\sigma_0$, $r_p = 3\sigma_0$, and segment length $L = 30\sigma_0$, as a function of Monte Carlo time t. The driving field strength is $f\sigma_0^3 = 0.07k_BT$.

value which is roughly independent of the pore size. The threshold driving field f^*, at which the crossover from small to large mobilities occurs, moves to larger values of f with increasing pore size. This qualitative behavior is very similar to the one observed experimentally [14,22].

A reasonably good collapse of data for different pore radii, bending rigidities, and vesicle sizes can be obtained by using a rescaled driving field $\tilde{f} = f/f^*$. Dimensional analysis leads us to expect that f^* should have the scaling form

$$f^* = \kappa A^{-3/2}\, \Xi\left(\frac{\sqrt{A}}{r_p}, \frac{\xi_p}{\sqrt{A}}, \frac{\kappa}{k_B T}\right) , \qquad (5)$$

where $A \sim \sigma_0^2 N$. The scaling function Ξ depends on $\kappa/(k_B T)$, and on two ratios of three length scales, the pore radius r_p, the vesicle radius $r_v \sim \sqrt{A}$, and the persistence length $\xi_p = a_0 \exp[(4\pi/3)\kappa/(k_B T)]$ (where a_0 is a microscopic length scale of order σ_0) [24,25]. In the limit of large bending rigidities, where $\xi_p \gg r_p$, the scaling form (5) reduces to

$$f^* = \kappa A^{-3/2}\, \Xi_\infty\left(\frac{\sqrt{A}}{r_p}, \frac{\kappa}{k_B T}\right) . \qquad (6)$$

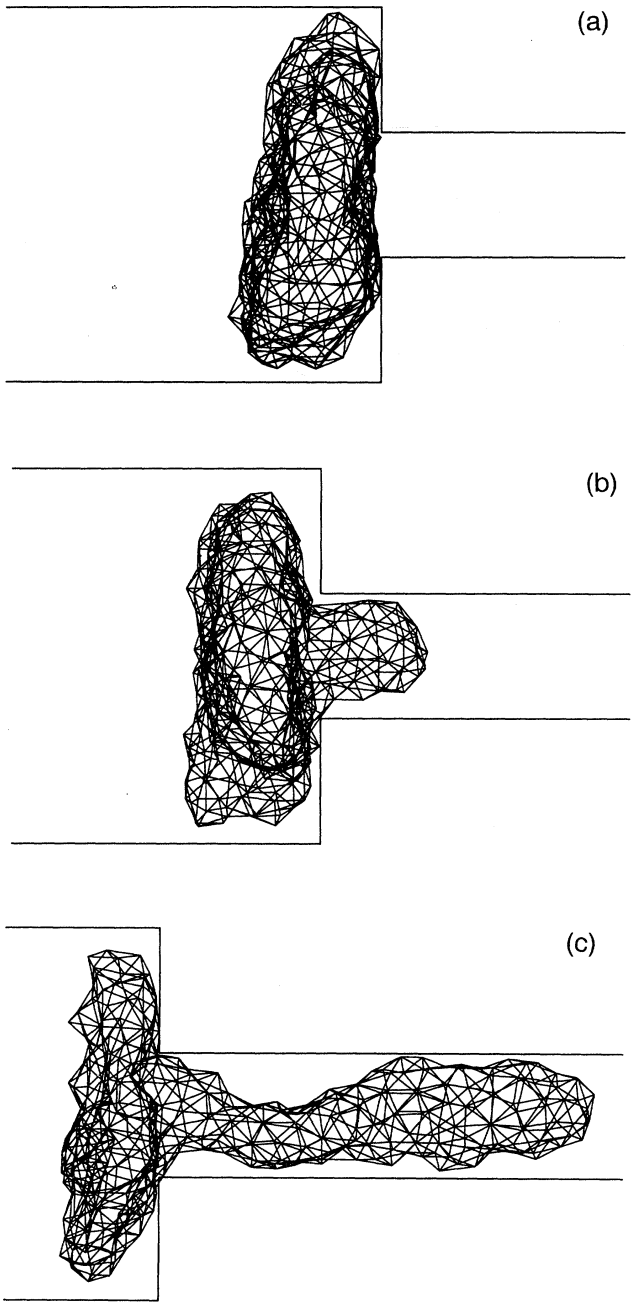

FIG. 2. Conformations of a vesicle of size $N = 407$ and bending rigidity $\lambda = 2.0 k_B T$ moving in a tube of radius $R = 9\sigma_0$ at three different stages of squeezing through a cylindrical pore of radius $r_p = 3.0\sigma_0$. (a) $f\sigma_0^3 = 0.06 k_B T$, after 10×10^6 MCS, (b) $f\sigma_0^3 = 0.06 k_B T$, after 30×10^6 MCS, (c) $f\sigma_0^3 = 0.09 k_B T$, after 10×10^6 MCS.

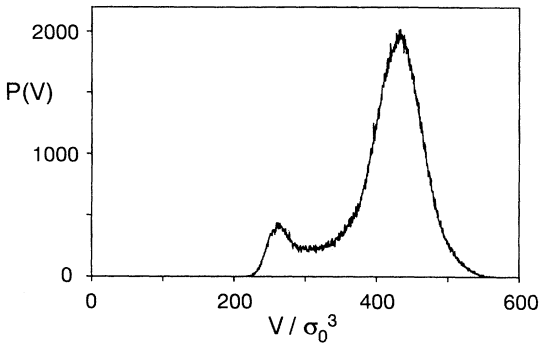

FIG. 3. Volume distribution function $P(V)$ for a vesicle of size $N = 247$ and bending rigidity $\lambda = 2.0 k_B T$, with pore size $r_p = 2.5\sigma_0$, segment length $L = 30\sigma_0$, tube radius $R = 7\sigma_0$, and driving field $f\sigma_0^3 = 0.09 k_B T$.

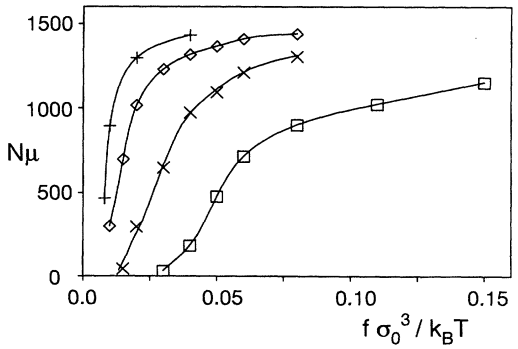

FIG. 4. The reduced mobility $N\mu$ [measured in units of $\sigma_0^2/(k_B T)$ per 10^6 MCS] of a vesicle of rigidity $\lambda = 1.0 k_B T$ as a function of the driving field strength $f\sigma_0^3/(k_B T)$, for four different pore radii r_p, as indicated. The length of the tube segments is $L = 15\sigma_0$; the radius of the wide parts of the tube is $R = 5\sigma_0$.

A more detailed justification of this scaling ansatz will be given in Sec. III. Using the results of Secs. III and IV as a guide, we have analyzed our data using a simple power-law ansatz

$$f^*/k_BT = f_0\ (\kappa/k_BT)^{1+\beta}\ A^{-3/2+\eta}\ r_p^{-2\eta}\ . \qquad (7)$$

Scaling plots for fixed λ and various values of r_p and N are shown in Fig. 5. Scaling plots for fixed r_p with different values of λ and N are shown in Fig. 6. Note that we have dropped the λ dependence of f^* in Fig. 5, and the r_p dependence of f^* in Fig. 6, so that the crossover from small to large mobility does not necessarily occur at similar values of f/f^* in these two figures. It can be seen from these figures (and Table I) that essentially all our data can be described consistently using the exponents $\beta = 0.2 \pm 0.2$ and $\eta = 2.4 \pm 0.1$. The only exception is the data set for $\lambda = 1.0k_BT$; however, this value of λ already lies in the regime of branched-polymer-like conformations [23,26] so that a different scaling behavior can be expected in this case, compare Eq. (5). It should be emphasized that β and η in Eq. (7) are effective exponents, which describe the data over the investigated range of parameters. These results probably do not represent true asymptotic scaling behavior.

The reason for this is that there are several sources of corrections to scaling. These corrections arise because in addition to r_p and $r_v \sim \sqrt{A}$ there are several other length scales in the simulations, such as the bead size σ_0, the tether length ℓ_0, and the tube radius R, which are not small (or large) compared to r_p and r_v [as they should be if the scaling law (5) is to be correct]. Consider, for example, the effect of the radius R of the wide parts of the tube. If R is too small, the vesicle cannot extend laterally as it is pressed against the entrance of a pore. On the other hand, if R is too large, the vesicle may not feel the pore immediately, but first have to diffuse laterally to reach the pore. The mobility curves for two different radii R, but otherwise identical systems are shown in Fig. 7. Fortunately, it turns out that there seems to be a range of R values, over which the dependence of the mobility on R is rather weak. Consider now the effect of changing the length L of the narrow and wide regions of the tube. Since the drift of the vesicle inside these tube segments does not provide any interesting information, we want to keep the segment length as small as possible in order to save simulation time. On the other hand, the vesicles can become quite elongated when they have to squeeze through a narrow pore. Therefore, if L is not large enough, the front end of the vesicle may already encounter the next pore while the vesicle is still elongated. In this case, it enters the pore more easily, and the mobility increases ("channeling"). In order to avoid this effect, we have used two values, $L = 15\sigma_0$ and $L = 30\sigma_0$,

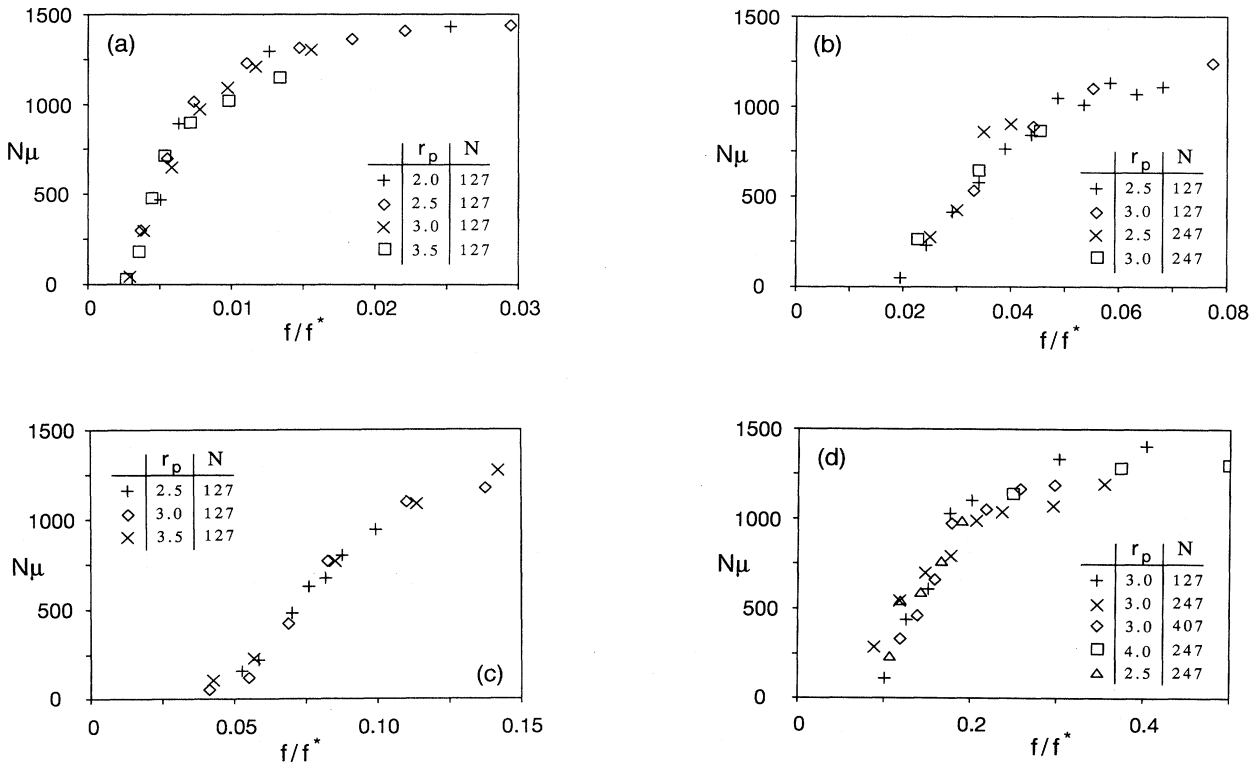

FIG. 5. Scaling plots of the reduced mobility $N\mu$ [measured in units of $\sigma_0^2/(k_BT)$ per 10^6 MCS] for fixed λ and several different N and r_p/σ_0, as indicated. (a) $\lambda = 1.0k_BT$, $L = 15\sigma_0$, (b) $\lambda = 2.0k_BT$, $L = 15\sigma_0$, (c) $\lambda = 3.0k_BT$, $L = 15\sigma_0$, (d) $\lambda = 2.0k_BT$, $L = 30\sigma_0$. The tube radius is $R = 5\sigma_0$ for $N = 127$, $R = 7\sigma_0$ for $N = 247$, and $R = 9\sigma_0$ for $N = 407$. Here, we use the form $f^*\sigma_0^3/k_BT = (r_p/\sigma_0)^{-2\eta_1} N^{-3/2+\eta_2}$ for the threshold field strength. The values of the effective exponents are listed in Table I.

for the segment length, compare Figs. 5 and 6; for the simulations of the largest vesicle size ($N = 407$) only the segment length $L = 30\sigma_0$ has been employed. Neither a visual inspection of a (small) number of vesicle conformations nor a comparison of the scaling behavior for different values of L give any indication that our results are affected by channeling.

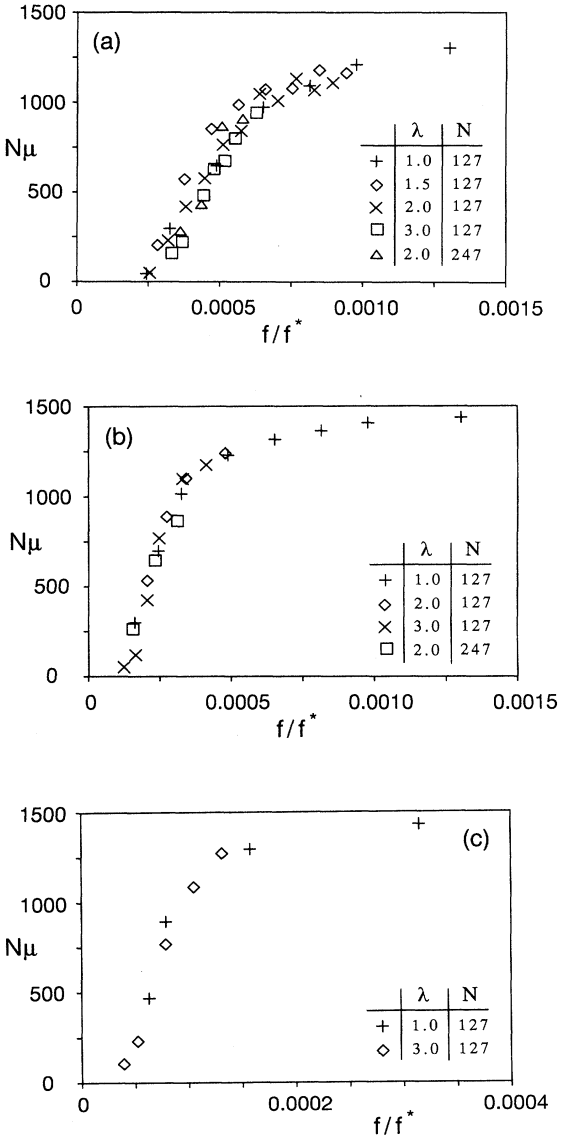

FIG. 6. Scaling plots of the reduced mobility $N\mu$ [measured in units of $\sigma_0^2/(k_BT)$ per 10^6 MCS] for fixed r_p and various N and λ/k_BT, as indicated. (a) $r_p = 2.5\sigma_0$, (b) $r_p = 3.0\sigma_0$, (c) $r_p = 3.5\sigma_0$. The segment length is $L = 15\sigma_0$ in all cases. The tube radius is $R = 5\sigma_0$ for $N = 127$, $R = 7\sigma_0$ for $N = 247$, and $R = 9\sigma_0$ for $N = 407$. Here, we use the form $f^*\sigma_0^3/k_BT = (\lambda/k_BT)^{1+\beta}N^{-3/2+\eta_2}$ for the threshold field strength. The values of the effective exponents are listed in Table I.

TABLE I. Effective exponents of the threshold field strength $f^*\sigma_0^3/k_BT \sim (\lambda/k_BT)^{1+\beta}(r_p/\sigma_0)^{-2\eta_1}N^{-3/2+\eta_2}$. For constant λ (Fig. 5), we use the threshold field strength $f_1^*\sigma_0^3/k_BT = (r_p/\sigma_0)^{-2\eta_1}N^{-3/2+\eta_2}$; for constant r_p (Fig. 6), the threshold field strength $f_2^*\sigma_0^3/k_BT = (\lambda/k_BT)^{1+\beta}N^{-3/2+\eta_2}$. If the scaling ansatz (6), (7) is correct, the effective exponents η_1 and η_2 should be identical. Parentheses around some values of η_2 indicate that these values have not been determined from this particular data set (because it contains only data for a single value of N), but are taken from Fig. 5(b).

Figure	λ/k_BT	r_p/σ_0	β	η_1	η_2
5(a)	1.0			1.75	(2.50)
5(b)	2.0			2.25	2.50
5(c)	3.0			2.35	(2.50)
5(d)	2.0			2.50	2.30
6(a)		2.5	0.35		2.35
6(b)		3.0	0.25		2.35
6(c)		3.5	0.00		(2.50)

III. TRANSPORT FOR LARGE BENDING RIGIDITIES

In order to understand the scaling behavior of the threshold field strength, we have to look in more detail at the balance between the bending energy and the driving field for a vesicle sitting at the entrance of a pore. The driving field has two effects; it not only pulls the membrane into the pore, but it also deforms the vesicle into a flattened droplet configuration. For small driving fields, the vesicle is only slightly deformed at equilibrium, and there is just a slight protrusion into the pore. This configuration is locally stable. If, however, due for example to a spontaneous thermal fluctuation, the vesicle were to extend into the pore a distance on the order of the pore radius, the vesicle can lower its free energy by being sucked into the pore. For small driving fields, transport occurs via a nucleation process. The nucleation barrier

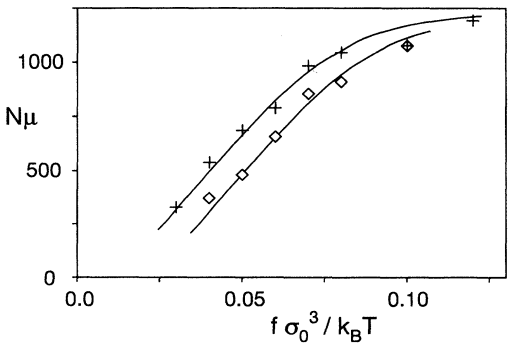

FIG. 7. The reduced mobility $N\mu$ [measured in units of $\sigma_0^2/(k_BT)$ per 10^6 MCS] as a function of the driving field $f\sigma_0^3/(k_BT)$ for $\lambda = 2.0\ k_BT$, $r_p = 3\sigma_0$, $L = 30\sigma_0$, and two different radii of the wide tube segments, $R = 7\sigma_0$ (+) and $R = 10\sigma_0$ ($\diamond$). The solid lines are guides to the eye.

decreases with increasing driving field strength, and eventually vanishes for sufficiently large fields. At this point, the permeability becomes independent of the strength of the driving field and the vesicle is sucked spontaneously into the pore.

A. Vesicles at a flat wall

Consider first the shape of a vesicle pressed against a flat wall located at $z = 0$ by the potential described by Eq. (2). For large bending rigidities, the shape of the vesicle can be determined by minimizing the total energy $F = F_b + F_p$ (with $F_b \equiv \mathcal{H}_{curv}$ and $F_p \equiv \mathcal{H}_{pot}$) for a given area A [27]. The fixed area constraint is incorporated by introducing a Lagrange multiplier Σ, as usual.

We restrict ourselves to axisymmetric shapes [9], so that solutions depend only on the arc length s along a meridian of the vesicle. The shape of the vesicle is then described by the tilt angle $\psi(s)$ and the coordinates $r(s)$ and $z(s)$, where r and z are the coordinates perpendicular and parallel to the axis of symmetry, respectively. The geometric relations between these coordinates are

$$\dot{r} = \cos(\psi), \tag{8}$$

$$\dot{z} = -\sin(\psi). \tag{9}$$

In this parametrization, the principal curvatures C_1 and C_2 are

$$C_1 = \dot{\psi}, \tag{10}$$

$$C_2 = \sin(\psi)/r, \tag{11}$$

where a dot denotes the derivative with respect to the arc length s. The total energy becomes

$$F = 2\pi\kappa \int_0^{s_1} L(\psi, \dot{\psi}, r, \dot{r}, z, \dot{z}, \gamma, \delta)\, ds + \pi\Sigma r^2(s_1), \tag{12}$$

with

$$L = \frac{r}{2}\left[\dot{\psi} + \frac{\sin(\psi)}{r}\right]^2 + \bar{\Sigma} r + \bar{f} r z + \gamma[\dot{r} - \cos(\psi)] + \delta[\dot{z} + \sin(\psi)], \tag{13}$$

where $\bar{\Sigma} \equiv \Sigma/\kappa$ and $\bar{f} \equiv f/\kappa$. The last two terms in Eq. (13), which involve the Lagrange multipliers $\gamma(s)$ and $\delta(s)$, have been introduced to guarantee that Eqs. (8) and (9) are fulfilled. The upper limit in the integral in Eq. (12) is the arc length s_1 at which the vesicle comes in contact with the wall.

The Euler-Lagrange equations for the vesicle shape are

$$\dot{\psi} = u, \tag{14}$$

$$\dot{u} = -\frac{u}{r}\cos(\psi) + \frac{\cos(\psi)\sin(\psi)}{r^2} + \frac{\gamma}{r}\sin(\psi) + \frac{\delta}{r}\cos(\psi), \tag{15}$$

$$\dot{\gamma} = \frac{1}{2}u^2 - \frac{\sin^2(\psi)}{r^2} + \bar{\Sigma} + \bar{f} z, \tag{16}$$

$$\dot{\delta} = \bar{f} r, \tag{17}$$

as well as Eqs. (8) and (9). The boundary conditions

$$r(0) = 0, \tag{18}$$

$$\psi(0) = 0, \tag{19}$$

$$\psi(s_1) = \pi, \tag{20}$$

$$z(s_1) = 0 \tag{21}$$

are obvious. The other boundary conditions are a bit more subtle [9]. Because $\partial L/\partial s = 0$, the Hamiltonian $H \equiv \dot{\psi}\partial L/\partial\dot{\psi} + \dot{r}\partial L/\partial\dot{r} + \dot{z}\partial L/\partial\dot{z} - L$ is conserved. Since the length of the integration interval s_1 is not fixed, extremizing F implies [28] $H(s_1) = 0$. Using this, one finds the additional boundary conditions [27]

$$\delta(0) = 0, \tag{22}$$

$$\gamma(0) = 0, \tag{23}$$

$$u(s_1) = 0, \tag{24}$$

$$\gamma(s_1) + \bar{\Sigma} r(s_1) = 0. \tag{25}$$

To determine the vesicle shape, we have integrated these equations using a fourth-order Runge-Kutta integration scheme with step size $\epsilon = 5 \times 10^{-3}$ for vesicles of area $A = 150$ and $A = 300$. $\bar{\Sigma}$, as well as the initial conditions $u(0)$ and $z(0)$ were then adjusted until the boundary conditions (20), (21), and (25), as well as the area constraint, are satisfied.

Since $\bar{f}$ has the dimensions of inverse length cubed, and $A^{1/2}$ is the only length scale in the problem, we expect F/κ to depend only on the product $\bar{f}A^{3/2}$. This is indeed borne out by our results. Figure 8 contains a plot of our data for $\bar{F}_v \equiv F/(2\pi\kappa)$ vs $\bar{f}A_0^{3/2}$ obtained using both $A_0 = 150$ and $A_0 = 300$. We have not gone beyond $\bar{f}A_0^{3/2} \approx 700$ since the dimple at the vesicle center intersects the substrate for larger values of this parameter.

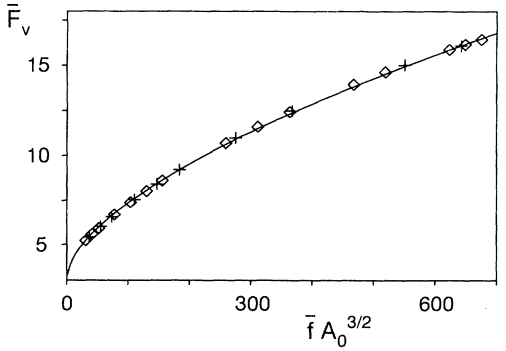

FIG. 8. Reduced vesicle free energy $\bar{F}_v \equiv F_v/(2\pi\kappa)$ vs $\bar{f}A_0^{3/2}$ for $A_0 = 150$ (+) and $A_0 = 300$ (◇). The solid line is a plot of $\bar{F}_v = 3.2 + 0.25(\bar{f}A_0^{3/2})^{0.61}$.

For the plotted parameter range, we find that

$$\bar{F}_v \approx 3.2 + 0.25(\bar{f}A_0^{3/2})^{\zeta}\ , \tag{26}$$

with $\zeta \simeq 0.61$. Some insight into the origins of this scaling behavior can be obtained from the analysis of a simple flattened droplet model for the adsorbed vesicle given in the Appendix.

B. The pore region: Small amplitude results

The same procedure can be used to study the portion of the membrane in the pore region. Consider a large, flat membrane located at $z = 0$. At the origin there is a pore of radius r_p. Under the influence of the driving field, a portion of the membrane will be sucked into the pore. The shape of this deformed piece of membrane can be determined as in the preceding subsection. In particular, we want to determine the free energy of the membrane as a function of the field $\bar{f}$, the pore radius r_p, and the excess area ΔA, where ΔA is equal to the area of the membrane in the region $r < r_p$ minus the pore area πr_p^2.

The limit of small deviations from planarity can be analyzed exactly. To lowest order in the out-of-plane displacement $z(r)$, the free energy is given by

$$F/2\pi\kappa \simeq \frac{1}{2}\int_0^{r_p} rdr\ (\nabla^2 z)^2 + \frac{1}{2}\bar{\Sigma}\int_0^{r_p} rdr\ (\nabla z)^2 + \bar{f}\int_0^{r_p} rdr\ z. \tag{27}$$

The Euler-Lagrange equation is

$$\nabla^4 z - \bar{\Sigma}\nabla^2 z + \bar{f} = 0, \tag{28}$$

with the boundary conditions $z(r_p) = 0$ and $z'(r_p) = 0$, where the prime denotes the derivative with respect to r. The general (axisymmetric) solution of Eq. (28) is

$$z(r) = a + br^2 + c\,\mathcal{C}_0(\lambda r), \tag{29}$$

where $\mathcal{C}_0(\lambda r) = I_0(\lambda r)$ for $\bar{\Sigma} > 0$, $\mathcal{C}_0(\lambda r) = J_0(\lambda r)$ for $\bar{\Sigma} < 0$, and $\lambda^2 = |\Sigma|$. For $\bar{\Sigma} = 0$, the solution becomes $z(r) = a + br^2 + cr^4$. Explicitly,

$$z(r) = \pm\frac{\bar{f}}{4\lambda^2}(r^2 - r_p^2) - \frac{\bar{f}r_p}{2\lambda^3\mathcal{C}_1(\lambda r_p)}[\mathcal{C}_0(\lambda r) - \mathcal{C}_0(\lambda r_p)], \tag{30}$$

where the top sign corresponds to $\bar{\Sigma} > 0$ and the lower to $\bar{\Sigma} < 0$. Similarly, $\mathcal{C}_i$ is to be identified with the modified Bessel function I_i in the first case, and the Bessel function J_i in the second. The area increment ΔA is given by

$$\frac{\Delta A}{r_p^2} = \frac{\pi}{4}(\bar{f}r_p^3)^2\frac{1}{x^4}\left\{\frac{3}{4} \pm \left(\frac{2}{x} - \frac{\mathcal{C}_0(x)}{\mathcal{C}_1(x)}\right) \times \left(\frac{2}{x} + \frac{1}{2}\frac{\mathcal{C}_0(x)}{\mathcal{C}_1(x)}\right)\right\}, \tag{31}$$

where $x = \lambda r_p$. The potential energy F_p behaves as

$$\bar{F}_p \equiv F_p/2\pi\kappa = \frac{(\bar{f}r_p^3)^2}{4x^2}\left\{\mp\frac{1}{4} - \frac{2}{x^2} + \frac{1}{x}\frac{\mathcal{C}_0(x)}{\mathcal{C}_1(x)}\right\} \tag{32}$$

and the bending energy as

$$\bar{F}_b \equiv F_b/2\pi\kappa = \frac{(\bar{f}r_p^3)^2}{2x^4}\left\{-\frac{1}{2} + \frac{x^2}{8\mathcal{C}_1^2(x)}[\mathcal{C}_0^2(x) \mp \mathcal{C}_1^2(x)]\right\}. \tag{33}$$

These results show that both F_b and F_p scale as

$$F_{b/p} = \kappa(\bar{f}r_p^3)^2\mathcal{F}_{b/p}[(\Delta A/r_p^2)/(\bar{f}r_p^3)^2]. \tag{34}$$

Furthermore, expanding for small x, one finds that

$$\bar{F}_b \sim (\bar{f}r_p^3)^{2(1-2\alpha)}(\Delta A/r_p^2)^{2\alpha} \tag{35}$$

and

$$\bar{F}_p \sim -(\bar{f}r_p^3)^{2(1-\alpha)}(\Delta A/r_p^2)^{\alpha}, \tag{36}$$

with $\alpha = 15/32$. $x = 0$ corresponds to $(\Delta A/r_p^2)/(\bar{f}r_p^3)^2 = \pi/6144 \approx 5.1 \times 10^{-4}$. $\bar{\Sigma} > 0$ for smaller values of ΔA and $\bar{\Sigma} < 0$ corresponds to larger values of ΔA.

Plots of $\bar{F}_b/(\bar{f}r_p^3)^2$ and $-\bar{F}_p/(\bar{f}r_p^3)^2$ vs $(\Delta A/r_p^2)/(\bar{f}r_p^3)^2$ are shown in Figs. 9 and 10, respectively. It can be seen that there is a crossover from behavior characterized by Eqs. (35) and (36) for small values of $(\Delta A/r_p^2)/(\bar{f}r_p^3)^2$ to

$$\bar{F}_b \sim \Delta A/r_p^2 \tag{37}$$

and

$$\bar{F}_p \sim -\bar{f}r_p^3\sqrt{\Delta A/r_p^2}, \tag{38}$$

for larger values of the excess area.

C. The pore region: Arbitrary amplitudes

Results for arbitrary out-of-plane displacements are easily obtained by solving the Euler-Lagrange equations

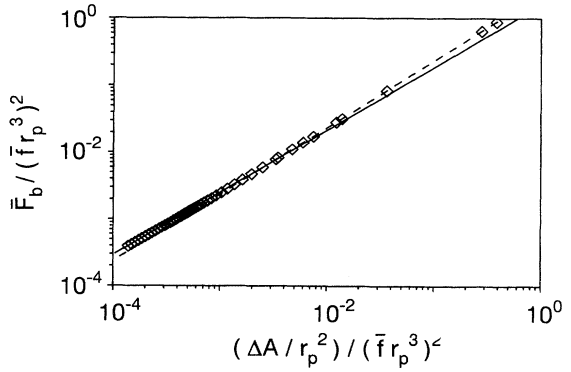

FIG. 9. $\bar{F}_b/(\bar{f}r_p^3)$ as a function of $(\Delta A/r_p^2)/(\bar{f}r_p^3)^2$. The scaling behavior is characterized by Eq. (35) for small values, and Eq. (37) for large values of the excess area.

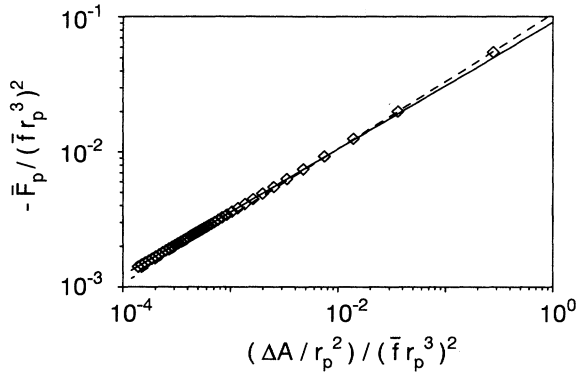

FIG. 10. $-\bar{F}_b/(\bar{f}r_p^3)^2$ as a function of $(\Delta A/r_p^2)/(\bar{f}r_p^3)^2$. The scaling behavior is characterized by Eq. (36) for small values, and Eq. (38) for large values of the excess area.

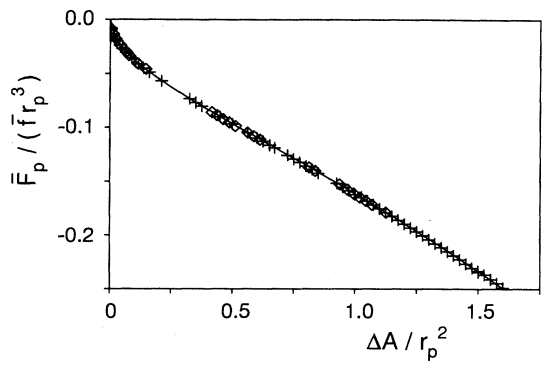

FIG. 12. Scaling plot of data for $\bar{F}_p/(\bar{f}r_p^3)$ obtained by solving the Euler-Lagrange equations for two values of the pore radius $r_p = 2$ (+) and 4 ($\diamond$). The solid line is a fit to the data [Eq. (43)].

(8), (9), and (14)–(16) numerically. This was done using the Runge-Kutta algorithm with step size $\epsilon = 5 \times 10^{-4}$ with the boundary conditions (18), (19), and (21)–(23), as well as

$$\psi(s_1) = 0, \tag{39}$$

$$r(s_1) = r_p, \tag{40}$$

$$\frac{1}{2}r(s_1)u^2(s_1) - \bar{\Sigma}r(s_1) = \gamma(s_1). \tag{41}$$

Solutions are obtained by adjusting $\bar{\Sigma}$, $u(0)$, and $z(0)$ until these boundary conditions as well as the excess area constraint are satisfied. In order to test scaling, solutions were obtained for two values of the pore radius, $r_p = 2$ and $r_p = 4$. It turns out that for the relevant range of parameters, the small amplitude scaling behavior is characterized by Eqs. (37) and (38). Using these results as a guide, we expect that $\bar{F}_b$ and $\bar{F}_p/(\bar{f}r_p^3)$ should depend only on $\Delta A/r_p^2$. We have therefore plotted our results for $\bar{F}_b$ and $\bar{F}_p/(\bar{f}r_p^3)$ vs $\Delta A/r_p^2$ in Figs. 11 and 12, respectively. The solid lines are fits to the data. In particular, we find that

$$\bar{F}_b \approx 2.5475x - 1.75x^2 + 1.26x^3 - 0.6x^4 + 0.12x^5 \tag{42}$$

and

$$\bar{F}_p \approx -(\bar{f}r_p^3)\sqrt{x}(0.1152 + 0.038\,16x + 0.008\,167\,6x^2), \tag{43}$$

where $x \equiv \Delta A/r_p^2$.

It is instructive to consider the behavior of $\bar{F}(\Delta A/r_p^2, \bar{f}r_p^3) = \bar{F}_b + \bar{F}_p$. The equilibrium configuration for a given value of f is determined by minimizing $\bar{F}$ with respect to ΔA. Figure 13 contains a plot of $\bar{F}$ as a function of $\Delta A/r_p^2$ for three values of $\bar{f}r_p^3$ obtained using (42) and (43). For $\bar{f}r_p^3 = 11$, there is a minimum at small $\Delta A/r_p^2$ and a peak at larger values of the reduced area. For $\bar{f}r_p^3 = 12.8$, the two extremal solutions have co-

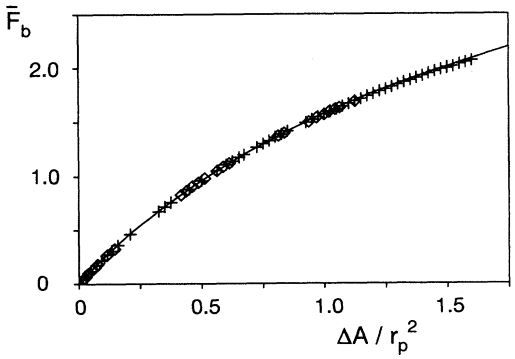

FIG. 11. Scaling plot of data for $\bar{F}_b$ obtained by solving the Euler-Lagrange equations for two values of the pore radius $r_p = 2$ (+) and $r_p = 4$ ($\diamond$). The solid line is a fit to the data [Eq. (42)].

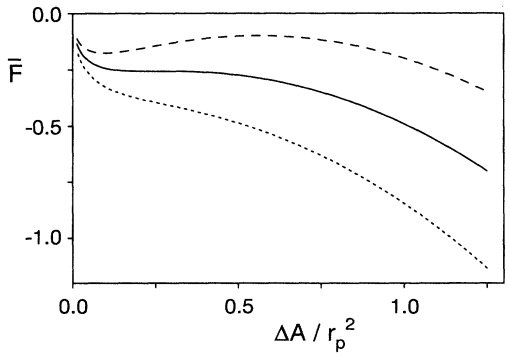

FIG. 13. The total free energy $\bar{F}$ as a function of $\Delta A/r_p^2$ for three values of $\bar{f}r_p^3$, using (42) and (43). For subcritical field strengths ($\bar{f}r_p^3 = 11$, dashed line), there is a metastable minimum at small values of $\Delta A/r_p^2$. This minimum vanishes for the critical field strength ($\bar{f}^* r_p^3 = 12.8$, solid line). For larger values f there is no minimum (dotted line); in this regime, the flat membrane is unstable and is spontaneously sucked into the pore.

alesced, and for higher field strengths, the free energy is a monotonically decreasing function of $\Delta A/r_p^2$. For small field strengths, therefore, the membrane protrudes only a small amount into the pore. However, spontaneous fluctuations of sufficient amplitude can push the membrane over the free energy barrier, causing the membrane to be sucked into the tube. The height of this nucleation barrier decreases with increasing field strength, ultimately vanishing at a critical field strength f^*. For larger values of the field, the flat membrane is unstable and is spontaneously sucked into the pore. The critical field strength scales as $f^* \sim \kappa r_p^{-3}$ in this case.

D. The vesicle-pore system

The behavior of the whole adsorbed vesicle-pore system can be determined in an analogous fashion. For simplicity, we assume that the reduced vesicle free energy $\bar{F}_v$ is given by (26). The total free energy is therefore

$$\bar{F}_t = 0.25[(\bar{f}\{A_0 - \Delta A\}^{3/2})^\zeta - (\bar{f}A_0^{3/2})^\zeta] + \bar{F}_b + \bar{F}_p, \tag{44}$$

where $\bar{F}_b$ and $\bar{F}_p$ are given by (42) and (43), respectively, and A_0 is the total surface area of the vesicle. We have subtracted off the reference free energy of the vesicle adsorbed on a flat wall so that $\bar{F}_t(\Delta A = 0) = 0$.

The critical field strength f^* at which the nucleation barrier vanishes is determined by the simultaneous solution of the two equations $\partial \bar{F}_t/\partial \Delta A = 0$ and $\partial^2 \bar{F}_t/\partial(\Delta A)^2 = 0$. It follows from Eqs. (42)–(44) that f^* has the scaling form

$$f^* = \kappa A_0^{-3/2} \Gamma(r_p^2/A_0) \ . \tag{45}$$

This result confirms the scaling ansatz which we have used to analyze our Monte Carlo data. Our numerical results for the scaled critical field strength $\bar{f}^* A_0^{3/2}$ are plotted in Fig. 14 as a function of r_p^2/A_0 for the two values $A_0 = 250$ and 500. It can be seen that $\bar{f}^* A_0^{3/2} \sim (r_p^2/A_0)^{-\eta}$, with $\eta \simeq 1.55$. This implies that the threshold field strength scales as $f^* \sim \kappa r_p^{-2\eta} A_0^{\eta - 3/2}$.

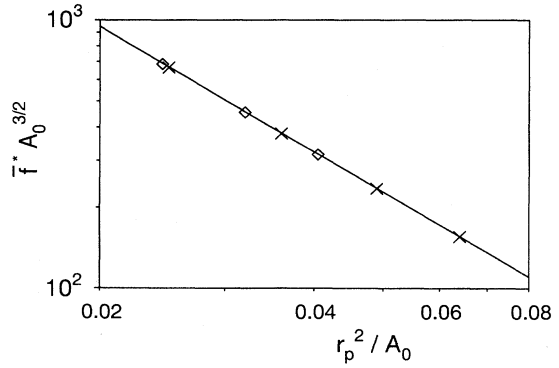

FIG. 14. Scaled critical field strength $\bar{f}^* A_0^{3/2}$ as a function of r_p^2/A_0 for the two values $A_0 = 250$ ($\times$) and 500 ($\diamond$). In the regime studied, $\bar{f}^* A_0^{3/2} \sim (r_p^2/A_0)^{-\eta}$, with $\eta \simeq 1.55$.

This calculation shows that for an ensemble of vesicles, where each is squeezed through a single pore, the value of the threshold field strength should *not* depend on the fate of the vesicle after penetration of the pore. The rate determining process is the nucleation of an initial, sufficiently large protrusion. Vesicle fragmentation inside the pore should therefore not affect the mobility (or permeability) curves.

IV. FLUCTUATION EFFECTS

Thermal fluctuations modify the results of the preceding section in several ways. First, the bending rigidity on large length scales is reduced by fluctuations. This can be taken into account by replacing κ in the free energy F_v of a vesicle of radius $r_v \sim \sqrt{A}$ by the renormalized rigidity [25,29,30,26]

$$\kappa_R(r_v) = \kappa - \frac{3k_BT}{4\pi} \ln(r_v/a_0) \ , \tag{46}$$

where a_0 is a microscopic cutoff of the order of the size of the molecules. Similarly, κ in the pore contribution to the free energy has to be replaced by $\kappa_R(r_p)$. The effect of the reduced bending rigidity becomes pronounced when the persistence length approaches the vesicle size [so that $\kappa_R(r_v)$ becomes very small].

Second, membrane fluctuations lead to a steric repulsion between different parts of the vesicle, as well as of the vesicle and the wall. To study this effect in more detail, consider the flattened droplet model described in the Appendix. For large field strengths, the distance $2h$ between the upper and the lower part of the flattened droplet becomes rather small. In this case, the steric interaction [31] gives an additional contribution

$$F_{st} = c_1 \frac{(k_BT)^2}{\kappa} \frac{\pi r_0^2}{(2h)^2} \tag{47}$$

to the free energy, where r_0 is the radius of the contact area of the vesicle and the wall. For simplicity, we ignore finite size corrections in Eq. (47). Monte Carlo simulations imply $c_1 \simeq 0.11$ [32–34]. For sufficiently small thickness h, the bending energy of the rim of the flattened droplet is small compared to the steric repulsion. In this case, the free energy of the vesicle is (approximately)

$$F_v(x) = \frac{1}{\sqrt{2\pi}} f A^{3/2} x + \pi c_1 \frac{(k_BT)^2}{\kappa} x^{-2}, \tag{48}$$

where $x = h/r_0$. The minimization of Eq. (48) with respect to x gives

$$F_v = \frac{3}{2} \kappa c_1 \left[\bar{f} A^{3/2} \frac{k_BT}{\kappa c_1} \right]^{2/3} \ . \tag{49}$$

Two conclusions can be drawn from this result. (i) The exponent ζ of the vesicle free energy can be larger than the value of $\zeta \simeq 0.61$ obtained by minimizing the bending energy. (ii) Another scaling variable, $\kappa/(k_BT)$, appears in the scaling form of the threshold field strength [compare Eq. (45)]. Note, however, that since $\partial^2 F_v/\partial(\Delta A)^2 = 0$ when $\zeta = 2/3$, higher-order correction terms will play an important role in determining the scaling behavior of the threshold field strength when the scaling exponent ζ approaches 2/3.

V. SUMMARY AND DISCUSSION

We have studied the transport properties of vesicles through narrow pores, using Monte Carlo simulations, scaling arguments, and a minimization of the bending energy in an external field. We find that while there is essentially no transport for driving fields which are smaller than a threshold field strength f^*, the vesicles move through the pores almost unhindered for driving fields larger than f^*. For small f, transport occurs via a nucleation process. With increasing f, the height of the nucleation barrier decreases and eventually vanishes at the critical field strength f^*. The threshold field increases with decreasing pore radius r_p as well as increasing bending rigidity κ and membrane area. This general behavior is in agreement with experiment [13]. The roughly linear dependence of f^* on κ explains why ultraflexible vesicles are much more efficient than large-bending-rigidity liposomes for the transport of drugs through the intact skin: only for small bending rigidities can the regime $f > f^*$ be reached for realistic driving fields.

The present work should be extended in several directions. First, simulations should be performed at larger bending rigidities in order to check explicitly if the scaling behavior obtained in Sec. III is recovered. Second, the dependence of the mobility on the outer tube radius R has to be studied in more detail. In particular, it would be interesting to study the crossover from the diffusion- to the nucleation-dominated regime. Third, in order to understand the crossover from large to small κ, the transport properties of very-low-bending-rigidity vesicles (with $\kappa \ll k_BT$), which are characterized by branched-polymer-like conformations, have to be determined. Finally, the effect of the two-component nature of the lipid bilayer vesicles used in experiments has to be studied more carefully.

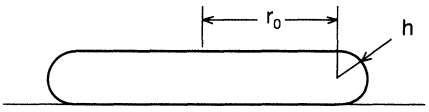

FIG. 15. Flattened droplet configuration of an adsorbed vesicle.

ACKNOWLEDGMENTS

Stimulating discussions with G. Cevc are gratefully acknowledged. This work was supported in part by the Deutsche Forschungsgemeinschaft through Sonderforschungsbereich 266, the National Science Foundation under Grant No. DMR-9405824, the donors of The Petroleum Research Fund, administered by the ACS, the University of Minnesota Army High Performance Computing Research Center, U.S. Army Contract No. DAAL03-89-C-0038, and NATO Grant No. CRG910156

APPENDIX: FLATTENED DROPLET MODEL

If the adsorbed vesicle is assumed to have the shape of a flattened droplet of thickness $2h$ and radius $r_0 + h$ (see Fig. 15), the vesicle free energy can be calculated explicitly. In this case, the total surface area of the vesicle is $A = 2\pi r_0^2(1 + \pi x + 2x^2)$,

$$F_b = 2\pi\kappa \left[4 + \frac{1}{x\sqrt{1-x^2}} \arccos(x)\right], \tag{A1}$$

and

$$F_p = 2\pi f r_0^3 x(1 + \pi x + 2x^2) \tag{A2}$$

$$= \frac{1}{\sqrt{2\pi}} f A^{3/2}\, x(1 + \pi x + 2x^2)^{-1/2}, \tag{A3}$$

where $x \equiv h/r_0$. The total energy $F = F_b + F_p$ is obtained by minimizing with respect to h. It follows that

$$F = 2\pi\kappa\, \Omega(\bar{f} A^{3/2}). \tag{A4}$$

The scaling behavior at large field strengths is easily determined by performing this calculation to lowest order in x. Explicitly, one finds that

$$\Omega(y) = 3 + (2\pi)^{-1/4}\sqrt{y} \tag{A5}$$

to leading order.

[1] *Statistical Mechanics of Membranes and Surfaces,* edited by D. Nelson, T. Piran, and S. Weinberg (World Scientific, Singapore, 1989).
[2] R. Lipowsky, Nature (London) **349**, 475 (1991).
[3] P.B. Canham, J. Theor. Biol. **26**, 61 (1970).
[4] W. Helfrich, Z. Naturforsch. Teil C **28**, 693 (1973).
[5] E. Evans, Biophys. J. **14**, 923 (1974).
[6] H.J. Deuling and W. Helfrich, J. Phys. (Paris) **37**, 1335 (1976).
[7] S. Svetina and B. Zeks, Eur. Biophys. J. **17**, 101 (1989).

[8] K. Berndl, J. Käs, R. Lipowsky, E. Sackmann, and U. Seifert, Europhys. Lett. **13**, 659 (1990).
[9] U. Seifert, K. Berndl, and R. Lipowsky, Phys. Rev. A **44**, 1182 (1991).
[10] L. Miao, U. Seifert, M. Wortis, and H.-G. Döbereiner, Phys. Rev. E **49**, 5389 (1994).
[11] T.L. Steck, in *Cell Shape: Determinants, Regulation, and Regulatory Role*, edited by W. Stein and F. Bronner (Academic, New York, 1989).
[12] G. Cevc and G. Blume, Biochim. Biophys. Acta **1104**, 226 (1992).
[13] G. Cevc, in *Structure and Dynamics of Membranes*, edited by R. Lipowsky and E. Sackmann, Handbook of Biological Physics Vol. 1 (Elsevier Science, Amsterdam, 1995).
[14] G. Cevc, D. Gebauer, A. Schätzlein, and G. Blume (unpublished).
[15] W. Harbich and W. Helfrich, Z. Naturforsch. Teil A **34**, 1063 (1979).
[16] R. Lipowsky and U. Seifert, Mol. Cryst. Liq. Cryst. **202**, 17 (1991).
[17] S. Leibler, J. Phys. (Paris) **47**, 507 (1986); S. Leibler and D. Andelman, *ibid.* **48**, 2013 (1987).
[18] S.A. Safran, P. Pincus, and D. Andelman, Science **248**, 354 (1990).
[19] U. Seifert, Phys. Rev. Lett. **70**, 1335 (1993).
[20] In order to avoid unwanted heating effects, the ion concentration in the solvent has to be very small in this case.
[21] G. Gompper and D.M. Kroll, Phys. Rev. Lett. **73**, 2139 (1994).
[22] G. Cevc, D. Gebauer, G. Gompper, and D.M. Kroll (unpublished).
[23] D.M. Kroll and G. Gompper, Science **255**, 968 (1992).
[24] P.-G. de Gennes and C. Taupin, J. Phys. Chem. **86**, 2294 (1982).
[25] L. Peliti and S. Leibler, Phys. Rev. Lett. **54**, 1690 (1985).
[26] G. Gompper and D.M. Kroll, Phys. Rev. E **51**, 514 (1995).
[27] U. Seifert and R. Lipowsky, Phys. Rev. A **42**, 4768 (1990).
[28] H. Goldstein, *Classical Mechanics* (Addison-Wesley, Reading, MA, 1965), p. 228.
[29] D. Förster, Phys. Lett. **114A**, 115 (1986).
[30] H. Kleinert, Phys. Lett. **114A**, 263 (1986).
[31] W. Helfrich, Z. Naturforsch. Teil A **33**, 305 (1978).
[32] G. Gompper and D.M. Kroll, Europhys. Lett. **9**, 59 (1989).
[33] W. Janke, H. Kleinert, and M. Meinhard, Phys. Lett. B **217**, 525 (1989).
[34] R. Netz and R. Lipowsky, Europhys. Lett. **29**, 345 (1995).